THE ASTROPHYSICAL JOURNAL, 494:317–335, 1998 February 10
© 1998. The American Astronomical Society. All rights reserved. Printed in U.S.A.

ON THE DIVERGENCE-FREE CONDITION AND CONSERVATION LAWS IN NUMERICAL SIMULATIONS FOR SUPERSONIC MAGNETOHYDRODYNAMIC FLOWS

WENLONG DAI AND PAUL R. WOODWARD
School of Physics and Astronomy/Laboratory for Computational Science and Engineering,
116 Church Street SE, Minneapolis, MN 55455
Received 1996 October 21; accepted 1997 September 4

ABSTRACT

An approach to maintain exactly the eight conservation laws and the divergence-free condition of magnetic fields is proposed for numerical simulations of multidimensional magnetohdyrodynamic (MHD) equations. The approach is simple and may be easily applied to both dimensionally split and unsplit Godunov schemes for supersonic MHD flows. The numerical schemes based on the approach are second-order accurate in both space and time if the original Godunov schemes are. As an example of such schemes, a scheme based on the approach and an approximate MHD Riemann solver is presented. The Riemann solver is simple and is used to approximately calculate the time-averaged flux. The correctness, accuracy, and robustness of the scheme are shown through numerical examples. A comparison in numerical solutions between the proposed scheme and a Godunov scheme without the divergence-free constraint implemented is presented.

Subject headings: methods: numerical — MHD — shock waves

1. INTRODUCTION

Godunov approaches for the magnetohydrodynamic (MHD) equations have been under development for many years. Brio & Wu (1988) applied Roe's method to the one-dimensional MHD equations Zachary & Colella (1992) and Zachary, Malagoli, & Colella (1994) applied the Engquist-Osher flux for hyperbolic systems of conservations laws to one- and multidimensional MHD equations. Dai & Woodward (1994a) developed a Riemann solver and extended the piecewise parabolic method (PPM) to multidimensional MHD equations (Dai & Woodward 1994b). Powell (1994) and Powell et al. (1995) developed a Roe-type Riemann solver and an upwind scheme for MHD equations using eight wave families. Ryu & Jones (1995), Ryu, Jones, & Frank (1995), and Balsara (1996) applied the TVD method to the MHD equations. Croisille, Kanfir, & Chanteur 1995 introduced a kinetic-type method for one-dimensional MHD equations. We would like to mention that Evan & Hawley (1988) developed a constrained transport method, and Stone & Norman (1992) incorporated the method in their MHD algorithms which have been relatively widely used in the astrophysics community.

These numerical schemes for MHD equations may obtain good results for some MHD problems, but questions remain in these schemes. In all these schemes for multidimensional MHD flows, either the conservation laws or the divergence-free condition of the magnetic field is satisfied only to the accuracy of schemes. In order to maintain the divergence-free condition exactly, one typical approach used in the existing Godunov schemes is to add a "clean-up" procedure after each time step (Balsara 1996; Ryu et al. 1995; Zachary et al. 1994). The clean-up was originally proposed for subsonic MHD flows and has been shown to work well (Brackbill & Barnes 1980). But when the clean-up is applied to supersonic MHD flows, new issues arise besides the CPU time needed for the Poisson equation after each time step. First, to solve the Poisson equation one needs global information, and global dependence of information is not favored in the existing parallel computers. Second, derivatives have to be directly evaluated for the divergence of the magnetic field. The evaluation of the derivatives may introduce $O(1)$ truncation errors near MHD discontinuities; therefore, although it seems that the solution from the clean-up satisfies the divergence-free condition, the value of the divergence is zero only to the accuracy of a numerical scheme. More seriously, the clean-up may destroy the conservative property of a Godunov scheme. As we know, the intermediate results for the magnetic field obtained before the clean-up is applied, together with the solutions for other variables, exactly satisfy the conservation laws. After the clean-up is applied, the magnetic field is modified, the conservation laws for the total energy and the three components of the magnetic field are satisfied only to the accuracy of the schemes, and truncation errors may be $O(1)$ near MHD discontinuities. This kind of $O(1)$ truncation errors may be easily detected when a strong MHD shock, propagating obliquely in a two-dimensional domain, is simulated using a nonconservative scheme.

In this paper, we propose an approach for numerical simulations of MHD flows in which both the conservation laws for mass, momentum, energy, and three components of magnetic fields, and the divergence-free condition are exactly satisfied. The approach is simple and may be easily applied to both dimensionally split and unsplit Godunov schemes for supersonic MHD flows. As an example, a scheme based on the approach and an approximate MHD Riemann solver is described in this paper. The scheme is simple compared to existing Godunov schemes for MHD flows. The plan of this paper is as follows. In § 2, an approach to exactly maintain the conservation laws and divergence-free condition is presented. Numerical schemes based on the approach and approximate MHD Riemann solvers are described in § 3. Numerical examples are given in § 4. The final section contains conclusions and a brief overview of this paper.

2. CONSERVATION LAWS AND THE DIVERGENCE-FREE CONDITION

The ideal MHD equations are (Landau & Lifshitz 1960)

$$\frac{\partial \rho}{\partial t} + \nabla \cdot (\rho \boldsymbol{u}) = 0 \,, \tag{1}$$

$$\rho\left(\frac{\partial \boldsymbol{u}}{\partial t} + \boldsymbol{u} \cdot \nabla \boldsymbol{u}\right) = -\nabla p + \frac{1}{4\pi} (\nabla \times \boldsymbol{B}) \times \boldsymbol{B} \,, \tag{2}$$

$$\frac{\partial}{\partial t}\left(\frac{1}{2}\,\rho \boldsymbol{u}^2 + \rho\epsilon + \frac{1}{8\pi}\,\boldsymbol{B}^2\right) = -\nabla \cdot \boldsymbol{q} \,, \tag{3}$$

$$\frac{\partial \boldsymbol{B}}{\partial t} = \nabla \times (\boldsymbol{u} \times \boldsymbol{B}) \,. \tag{4}$$

Here

$$\boldsymbol{q} \equiv \rho \boldsymbol{u}\left(\frac{1}{2}\,\boldsymbol{u}^2 + \epsilon + \frac{p}{\rho}\right) + \frac{1}{4\pi}\,\boldsymbol{B} \times (\boldsymbol{u} \times \boldsymbol{B}) \,,$$

and ρ, $\boldsymbol{u}$, p, $\boldsymbol{B}$, and ϵ are the mass density, flow velocity, thermal pressure, magnetic field, and specific internal energy. This set of equations is completed by the equation of state, for which we assume the gamma law: $p = (\gamma - 1)\rho\epsilon$. Here γ is the ratio of specific heats. The magnetic field $\boldsymbol{B}$ is assumed initially to be divergence-free. In this case, the above equations imply that it will remain divergence-free.

This set of equations may be written in the form of conservation laws:

$$\frac{\partial \boldsymbol{U}}{\partial t} + \frac{\partial \boldsymbol{F}_x}{\partial x} + \frac{\partial \boldsymbol{F}_y}{\partial y} + \frac{\partial \boldsymbol{F}_z}{\partial z} = 0 \,. \tag{5}$$

Here

$$\boldsymbol{U} \equiv \begin{pmatrix} \rho \\ \rho u_x \\ \rho u_y \\ \rho u_z \\ \rho e \\ B_x \\ B_y \\ B_z \end{pmatrix}, \qquad \boldsymbol{F}_x(\boldsymbol{U}) \equiv \begin{pmatrix} \rho u_x \\ \rho u_x u_x + P_{xx} \\ \rho u_x u_y + P_{xy} \\ \rho u_x u_z + P_{xz} \\ \rho u_x e + u_x P_{xx} + u_y P_{xy} + u_z P_{xz} \\ 0 \\ \Omega_z \\ -\Omega_y \end{pmatrix},$$

$$\boldsymbol{F}_y(\boldsymbol{U}) \equiv \begin{pmatrix} \rho u_y \\ \rho u_y u_x + P_{xy} \\ \rho u_y u_y + P_{yy} \\ \rho u_y u_z + P_{yz} \\ \rho u_y e + u_x P_{xy} + u_y P_{yy} + u_z P_{yz} \\ -\Omega_z \\ 0 \\ \Omega_z \end{pmatrix},$$

$$\boldsymbol{F}_z(\boldsymbol{U}) \equiv \begin{pmatrix} \rho u_z \\ \rho u_z u_x + P_{xz} \\ \rho u_z u_y + P_{yz} \\ \rho u_z u_z + P_{zz} \\ \rho u_z e + u_x P_{xz} + u_y P_{yz} + u_z P_{zz} \\ \Omega_y \\ -\Omega_x \\ 0 \end{pmatrix}.$$

In these definitions, $\boldsymbol{\Omega} \equiv \boldsymbol{u} \times \boldsymbol{B}$, e is the specific total energy, P_{xx}, P_{yy}, and P_{zz} are the diagonal elements of the total pressure tensor, P_{xy}, P_{xz}, and P_{yz} are the off-diagonal elements of the tensor, and they are defined as

$$e \equiv \epsilon + \frac{1}{2}u^2 + \frac{1}{8\pi\rho}\boldsymbol{B}^2 , \qquad P_{xx} \equiv p + \frac{1}{8\pi}(B_y^2 + B_z^2 - B_x^2) , \qquad P_{yy} \equiv p + \frac{1}{8\pi}(B_z^2 + B_x^2 - B_y^2) ,$$

$$P_{zz} \equiv p + \frac{1}{8\pi}(B_x^2 + B_y^2 - B_z^2) , \qquad P_{xy} \equiv -\frac{1}{4\pi}B_x B_y , \qquad P_{xz} \equiv -\frac{1}{4\pi}B_x B_z , \qquad P_{yz} = -\frac{1}{4\pi}B_y B_z .$$

Consider a numerical grid $\{x_i, y_j, z_k\}$ in a three-dimensional domain. Integrating equation (5) in a grid cell $x_i \le x \le x_{i+1}$, $y_j \le y \le y_{j+1}$, $z_k \le z \le z_{k+1}$ and over a time step $0 \le t \le \Delta t$ yields

$$\boldsymbol{U}_{i,j,k}(\Delta t) = \boldsymbol{U}_{i,j,k}(0) + \frac{\Delta t}{\Delta x_i}[\bar{\boldsymbol{F}}_{xj,k}(x_i) - \bar{\boldsymbol{F}}_{xj,k}(x_{i+1})] + \frac{\Delta t}{\Delta y_j}[\bar{\boldsymbol{F}}_{yi,k}(y_j) - \bar{\boldsymbol{F}}_{yi,k}(y_{j+1})] + \frac{\Delta t}{\Delta z_k}[\bar{\boldsymbol{F}}_{zi,j}(z_k) - \bar{\boldsymbol{F}}_{zi,j}(z_{k+1})] . \tag{6}$$

Here $\Delta x_i \equiv x_{i+1} - x_i$, $\Delta y_j \equiv y_{j+1} - y_j$, $\Delta z_k \equiv z_{k+1} - z_k$, $\boldsymbol{U}_{i,j,k}(t)$ is a cell-averaged value of $\boldsymbol{U}$ at time t, $\bar{\boldsymbol{F}}_{xj,k}(x_i)$ [or $\bar{\boldsymbol{F}}_{yi,k}(y_j)$, or $\bar{\boldsymbol{F}}_{zi,j}(z_k)$] is a time-averaged flux $\boldsymbol{F}_x$ (or $\boldsymbol{F}_y$ or $\boldsymbol{F}_z$) over the time step Δt at the cell interface $x = x_i$ (or $y = y_j$, or $z = z_k$), and they are defined as

$$\boldsymbol{U}_{i,j,k}(t) \equiv \frac{1}{\Delta x_i \Delta y_j \Delta z_k}\int_{z_k}^{z_{k+1}}\int_{y_j}^{y_{j+1}}\int_{x_i}^{x_{i+1}} \boldsymbol{U}(t, x, y, z)dx\,dy\,dz , \tag{7}$$

$$\bar{\boldsymbol{F}}_{xj,k}(x_i) \equiv \frac{1}{\Delta t \Delta y_j \Delta z_k}\int_0^{\Delta t}\int_{z_k}^{z_{k+1}}\int_{y_j}^{y_{j+1}} \boldsymbol{F}_x[\boldsymbol{U}(t, x_i, y, z)]dy\,dz\,dt , \tag{8}$$

$$\bar{\boldsymbol{F}}_{yi,k}(y_j) \equiv \frac{1}{\Delta t \Delta x_i \Delta z_k}\int_0^{\Delta t}\int_{z_k}^{z_{k+1}}\int_{x_i}^{x_{i+1}} \boldsymbol{F}_y[\boldsymbol{U}(t, x, y_j, z)dx\,dz\,dt , \tag{9}$$

$$\bar{\boldsymbol{F}}_{zi,j}(z_k) \equiv \frac{1}{\Delta t \Delta x_i \Delta y_j}\int_0^{\Delta t}\int_{y_j}^{y_{j+1}}\int_{x_i}^{x_{i+1}} \boldsymbol{F}_z[\boldsymbol{U}(t, x, y, z_k)dx\,dy\,dt . \tag{10}$$

We should mention that the difference equation (6) is exact. Although the time-averaged flux needed in equation (6) is always approximately calculated, the conservation laws for mass, momentum, energy, and three components of magnetic field are exactly satisfied in the difference equation (6).

In the difference equation (6), all the conserved quantities including the magnetic field $\boldsymbol{B}_{i,j,k}$ are defined as cell averages, equation (7). But the use of cell averages for the magnetic field is not natural in order to represent numerically the divergence-free constraint on the numerical representation of this field. Notice that the conservation laws for the magnetic field in any orthogonal coordinate system have a special feature. For example, the conservation law for B_x does not involve derivatives in the x-direction. It is this feature that makes it possible simultaneously to satisfy exactly eight conservation laws and the divergence-free condition in a set of eight difference equations. In order to show our numerical representation, we write $\boldsymbol{U}$ in a form

$$\boldsymbol{U} \equiv \begin{pmatrix} \boldsymbol{W} \\ \boldsymbol{B} \end{pmatrix} .$$

Here $\boldsymbol{W}$ contains the densities of mass, momentum, and total energy. In our scheme, five variables in $\boldsymbol{W}$ are represented by cell averages, equation (7), while the magnetic field is represented at interfaces of grid cells:

$$b_{xi,j,k} \equiv \frac{1}{\Delta y_j \Delta z_k}\int_{z_k}^{z_{k+1}}\int_{y_j}^{y_{j+1}} B_x(x_i, y, z)dy\,dz , \tag{11}$$

$$b_{yi,j,k} \equiv \frac{1}{\Delta x_j \Delta z_k}\int_{z_k}^{z_{k+1}}\int_{x_i}^{x_{i+1}} B_y(x, y_j, z)dx\,dz , \tag{12}$$

$$b_{zi,j,k} \equiv \frac{1}{\Delta x_j \Delta y_j}\int_{y_j}^{y_{j+1}}\int_{x_i}^{x_{i+1}} B_z(x, y, z_k)dx\,dy . \tag{13}$$

Notice that different components of the magnetic field are represented at different sets of interfaces. Value $\boldsymbol{b}_{i,j,k}$ is well defined even if a discontinuity surface of a fast shock (or a slow shock, or a rotational discontinuity, or a contact discontinuity) coincides with an interface of grid cells. Considering these averages at interfaces, we define a vector $\boldsymbol{V}_{i,j,k}$:

$$\boldsymbol{V}_{i,j,k} \equiv \begin{pmatrix} \boldsymbol{W}_{i,j,k} \\ \boldsymbol{b}_{i,j,k} \end{pmatrix} , \tag{14}$$

the elements of which have mixed definitions equations (7) and (11)–(13). In our scheme, the $\boldsymbol{V}_{i,j,k}$ are considered as independent variables which have to be updated, but the $\boldsymbol{B}_{i,j,k}$ are considered only as intermediate variables which are needed only for

an approximate calculation of the time-averaged fluxes needed in the scheme. The initial values of the $\boldsymbol{B}_{i,j,k}$ are calculated from $\boldsymbol{b}_{i,j,k}$ through definitions based on interpolations.

In our difference representation of the magnetic field, the net flux through the six interfaces of the grid cell is

$$\oint_{S_{i,j,k}} \boldsymbol{B} \cdot d\boldsymbol{s} = \Delta y_j \Delta z_k (b_{xi+1,j,k} - b_{xi,j,k}) + \Delta x_i \Delta z_k (b_{yi,j+1,k} - b_{yi,j,k}) + \Delta x_i \Delta y_j (b_{zi,j,k+1} - b_{zi,j,k}) .$$

Here $S_{i,j,k}$ stands for the surface of the grid cell. The divergence-free constraint on the magnetic field is exactly satisfied if and only if the equation

$$\Delta y_j \Delta z_k (b_{xi+1,j,k} - b_{xi,j,k}) + \Delta x_i \Delta z_k (b_{yi,j+1,k} - b_{yi,j,k}) + \Delta x_i \Delta y_j (b_{zi,j,k+1} - b_{zi,j,k}) = 0 \tag{15}$$

exactly holds for each grid cell.

For two-dimensional problems ($\partial/\partial z = 0$), $b_{zi,j,k} = B_{zi,j,k}$, and the divergence-free condition becomes

$$\Delta y_j (b_{xi+1,j,k} - b_{xi,j,k}) + \Delta x_i (b_{yi,j+1,k} - b_{yi,j,k}) = 0 . \tag{16}$$

As stated before, the averages of the magnetic field at three sets of interfaces, $\boldsymbol{b}_{i,j,k}$, are considered as independent variables in the approach. We integrate the three equations contained in equation (4), i.e., three equations for B_x, B_y, and B_z over the time step, and, respectively, at three interfaces $x = x_i$, $y = y_j$, and $z = z_k$ of a grid cell $x_i \le x \le x_{i+1}$, $y_j \le y < y_{j+1}$, and $z_k \le z \le z_{k+1}$. The integration gives us

$$b_{xi,j,k}(\Delta t) = b_{xi,j,k}(0) + \frac{\Delta t}{\Delta y_j} [\bar{\Omega}_{zk}(x_i, y_{j+1}) - \bar{\Omega}_{zk}(x_i, y_j)] - \frac{\Delta t}{\Delta z_k} [\bar{\Omega}_{yj}(x_i, z_{k+1}) - \bar{\Omega}_{yj}(x_i, z_k)] , \tag{17}$$

$$b_{yi,j,k}(\Delta t) = b_{yi,j,k}(0) + \frac{\Delta t}{\Delta z_k} [\bar{\Omega}_{xi}(y_j, z_{k+1}) - \bar{\Omega}_{xi}(y_j, z_k)] - \frac{\Delta t}{\Delta x_i} [\bar{\Omega}_{zk}(x_{i+1}, y_j) - \bar{\Omega}_{zk}(x_i, y_j)] , \tag{18}$$

$$b_{zi,j,k}(\Delta t) = b_{zi,j,k}(0) + \frac{\Delta t}{\Delta x_i} [\bar{\Omega}_{yj}(x_{i+1}, z_k) - \bar{\Omega}_{yj}(x_i, z_k)] - \frac{\Delta t}{\Delta y_j} [\bar{\Omega}_{xi}(y_{j+1}, z_k) - \bar{\Omega}_{xi}(y_j, z_k)] . \tag{19}$$

Here $\bar{\Omega}_{xi}$ (or $\bar{\Omega}_{yj}$, or $\bar{\Omega}_{zk}$) stands for a time-average along a line, i.e.,

$$\bar{\Omega}_{xi}(y_j, z_k) \equiv \frac{1}{\Delta t \Delta x_i} \int_0^{\Delta t} \int_{x_i}^{x_{i+1}} \Omega_x(x, y_j, z_k) dx\, dt , \tag{20}$$

$$\bar{\Omega}_{yj}(x_i, z_k) \equiv \frac{1}{\Delta t \Delta y_j} \int_0^{\Delta t} \int_{y_j}^{y_{j+1}} \Omega_y(x_i, y, z_k) dy\, dt , \tag{21}$$

$$\bar{\Omega}_{zk}(x_i, y_j) \equiv \frac{1}{\Delta t \Delta z_k} \int_0^{\Delta t} \int_{z_k}^{z_{k+1}} \Omega_z(x_i, y_j, z) dz\, dt . \tag{22}$$

We should mention that equations (17)–(19) are exact. From equations (17)–(19), it is easy to verify that the net magnetic flux across six interfaces of the grid cell is exactly maintained, i.e.,

$$\oint_{S_{i,j,k}} \boldsymbol{B}(\Delta t) \cdot d\boldsymbol{s} = \oint_{S_{i,j,k}} \boldsymbol{B}(0) \cdot d\boldsymbol{s} . \tag{23}$$

For two-dimensional problems ($\partial/\partial z = 0$), $b_{zi,j,k}$ is exactly same defined as $B_{zi,j,k}$, which is updated according to equation (6). Values $b_{xi,j}$ and $b_{yi,j}$ are updated according to

$$b_{xi,j}(\Delta t) = b_{xi,j}(0) + \frac{\Delta t}{\Delta y_j} [\bar{\Omega}_z(x_i, y_{j+1}) - \bar{\Omega}_z(x_i, y_j)] , \tag{24}$$

$$b_{yi,j}(\Delta t) = b_{yi,j}(0) - \frac{\Delta t}{\Delta x_i} [\bar{\Omega}_z(x_{i+1}, y_j) - \bar{\Omega}_z(x_i, y_j)] , \tag{25}$$

Here

$$\bar{\Omega}_z(x_i, y_j) \equiv \frac{1}{\Delta t} \int_0^{\Delta t} \Omega_z(x_i, y_j) dt .$$

Again, equations (24) and (25) are exact.

Although the flow variables $\boldsymbol{W}_{i,j,k}$ may be updated using either a dimensionally split or unsplit technique, the magnetic field $\boldsymbol{b}_{i,j,k}$ should be updated in an unsplit manner in order to exactly maintain the divergence-free constraint. We should point out

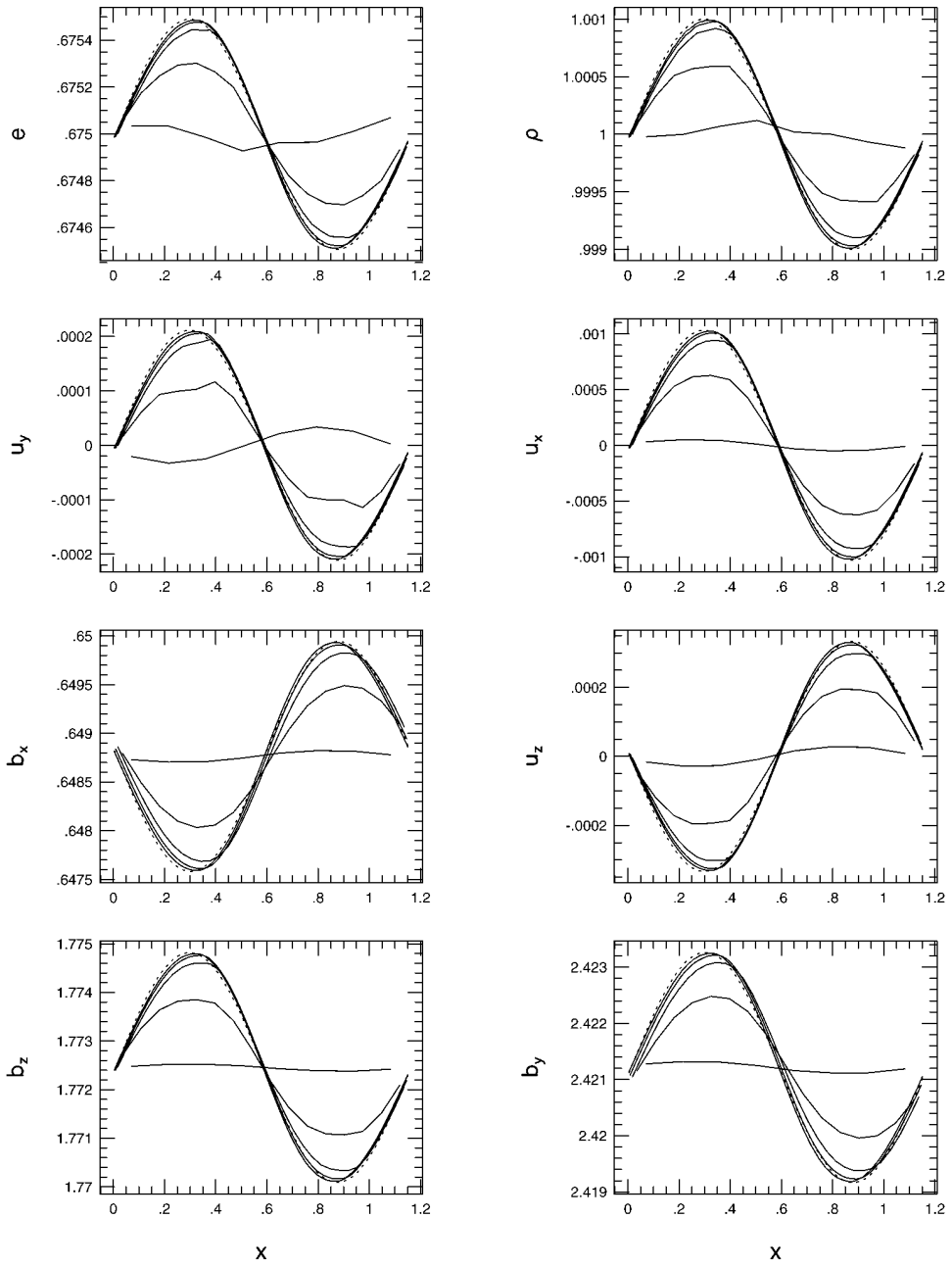

FIG. 1.—Fast wave propagating in a two-dimensional domain ($L_x - 0$) × ($L_y - 0$). Dashed lines are the profiles along the line $y = L_y/2$, and solid lines are the results at $t = 10$ obtained when five grids are used, which contain 128 × 128, 64 × 64, 32 × 32, 16 × 16, and 8 × 8 grid cells. The fast wave speed in the direction of wave propagation is very close to unity.

that the divergence-free condition is also exactly satisfied in the constrained transport method (Evans & Hawley 1988; Stone & Norman 1992).

2.1. *Numerical Schemes*

The approach proposed in the last section may be applied to both dimensionally split and unsplit Godunov schemes. We use the operator $D_{\Delta t}$ to represent the operation shown by equations (17)–(19) (or eqs. [24] and [25] for the two-dimensional situation). If $D_{\Delta t}$ is used together with an unsplit scheme $L_{\Delta t}$, such as those in Colella (1994) and Saltzman (1994), the resulting scheme may be written in the form

$$V_{i,j,k}(\Delta t) = D_{\Delta t} L_{\Delta t} V_{i,j,k}(0) .$$

The operator $D_{\Delta t}$ may also be applied to dimensionally split Godunov schemes. As we know, the cell averages $U_{i,j,k}$ may be updated using the dimensionally split technique (Stang 1968) for multidimensional problems. Each time step of a multidimen-

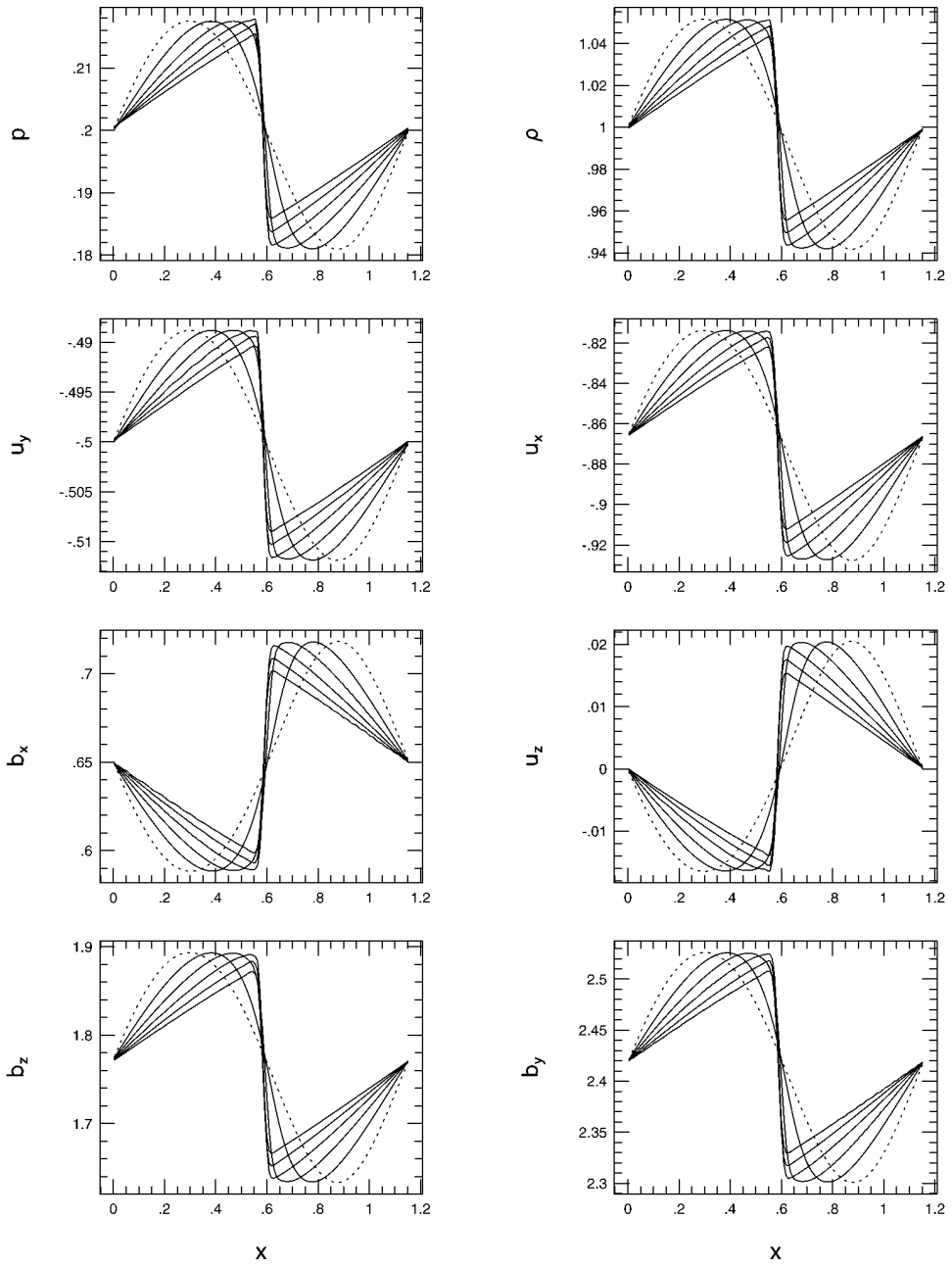

FIG. 2.—Nonlinear fast wave propagating in a two-dimensional domain ($L_x - 0$) × ($L_y - 0$). Dashed lines are the profiles along the line $y = L_y/2$, and solid lines are the profiles along the line at $t = 1, 2, 3, 4, 5$, which are obtained when 128 × 128 grid cells are used. The fast wave speed in the direction of wave propagation is very close to unity.

sional problem may be broken down into one-dimensional problems. Each time step of a multidimensional problem may be broken down into one-dimenional passes in which derivatives in other dimensions are set to zero. The dimensionally split technique may be written in the form

$$\boldsymbol{U}_{i,j,k}(2\,\Delta t) = L^x_{\Delta t} L^y_{\Delta t} L^z_{\Delta t} L^z_{\Delta t} L^y_{\Delta t} L^x_{\Delta t}\, \boldsymbol{U}_{i,j,k}(0)\ . \tag{26}$$

Here $L^x_{\Delta t}$ is a one-dimensional operator in the x-direction with the time step Δt. If the one-dimensional operator is second-order accurate, then the scheme constructed as equation (26) is second-order accurate, too. If we applied the operator $D_{\Delta t}$ in the scheme equation (26), we may write the scheme as

$$\boldsymbol{V}_{i,j,k}(2\,\Delta t) = D_{\Delta t} L^x_{\Delta t} L^y_{\Delta t} L^z_{\Delta t} D_{\Delta t} L^z_{\Delta t} L^y_{\Delta t} L^x_{\Delta t}\, \boldsymbol{V}_{i,j,k}(0)\ . \tag{27}$$

As an example, we develop a second-order scheme which is based on the dimensionally split technique in equation (26) and an approximate MHD Riemann solver. Therefore, the numerical results to be presented in the next section are obtained through one of the schemes, equation (27). The time-averaged flux needed in a one-dimensional pass is calculated through an approximate MHD Riemann solver. The Riemann solver used in our scheme is an extension of the solver described

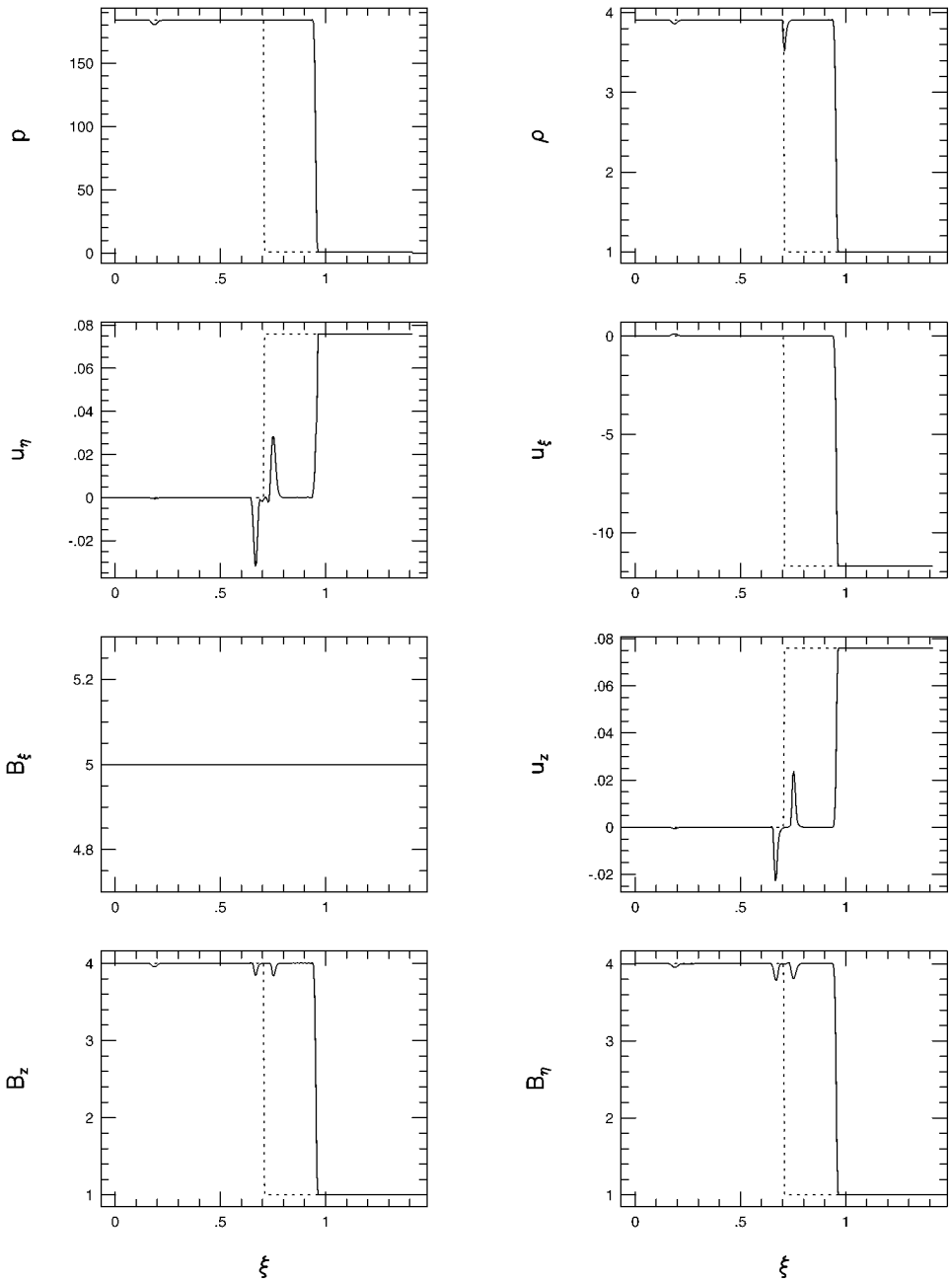

FIG. 3.—Shock-tube problem in a two-dimensional domain. The initial condition along the ξ-direction is shown by the dashed lines, which are exactly the same as that in Fig. 1. The ξ-direction makes an angle $\alpha = 45°$ with the x-axis. $B_\xi = 5$. Solid lines are the profiles at $t = 0.06$.

in Dai & Woodward (1994c) to the single-step Eulerian formulations, which is based on characteristic formulations for MHD equations. The initial $\boldsymbol{B}_{i,j,k}$ may be approximately obtained through the approximation

$$B_{xi,j,k} \approx \tfrac{1}{2}(b_{xi+1,j,k} + b_{xi,j,k}) , \qquad B_{yi,j,k} \approx \tfrac{1}{2}(b_{yi,j+1,k} + b_{yi,j,k}) , \qquad B_{zi,j,k} \approx \tfrac{1}{2}(b_{zi,j,k+1} + b_{zi,j,k}) .$$

We use the dimensionally split technique equation (26) to update the cell-averaged quantities, $\boldsymbol{W}_{i,j,k}$ and $\boldsymbol{B}_{i,j,k}$. The results from the operation equation (26) are numerical solutions accurate to the second order. But the solution for $\boldsymbol{B}_{i,j,k}$ obtained from equation (26) does not exactly satisfy the divergence-free condition. Therefore, in our scheme, the cell-averaged $\boldsymbol{B}_{i,j,k}$ updated through equation (26) is used only for an approximate calculation of the time-averaged flux needed in equations (17)–(19), (24) and (25).

Our one-dimensional functioning code starts from the cell-averages of a set of variables ($\rho, \rho u_x, \rho u_y, p u_z, \rho e, B_x, B_y, B_z$). For purely one-dimensional MHD flows, $\boldsymbol{B}_{i,j,k}$ is exactly the same as $\boldsymbol{b}_{i,j,k}$, but initial $\boldsymbol{B}_{i,j,k}$ is approximately calculated from $\boldsymbol{b}_{i,j,k}$ in our multidimensional scheme. Other variables, such as thermal pressure and internal energy, are approximately derived from this set of variables. For each variable, interpolations are used to determine the structure of the variable inside each grid cell. Although more sophisticated interpolations may be used, we use the linear interpolation in this paper for the cell

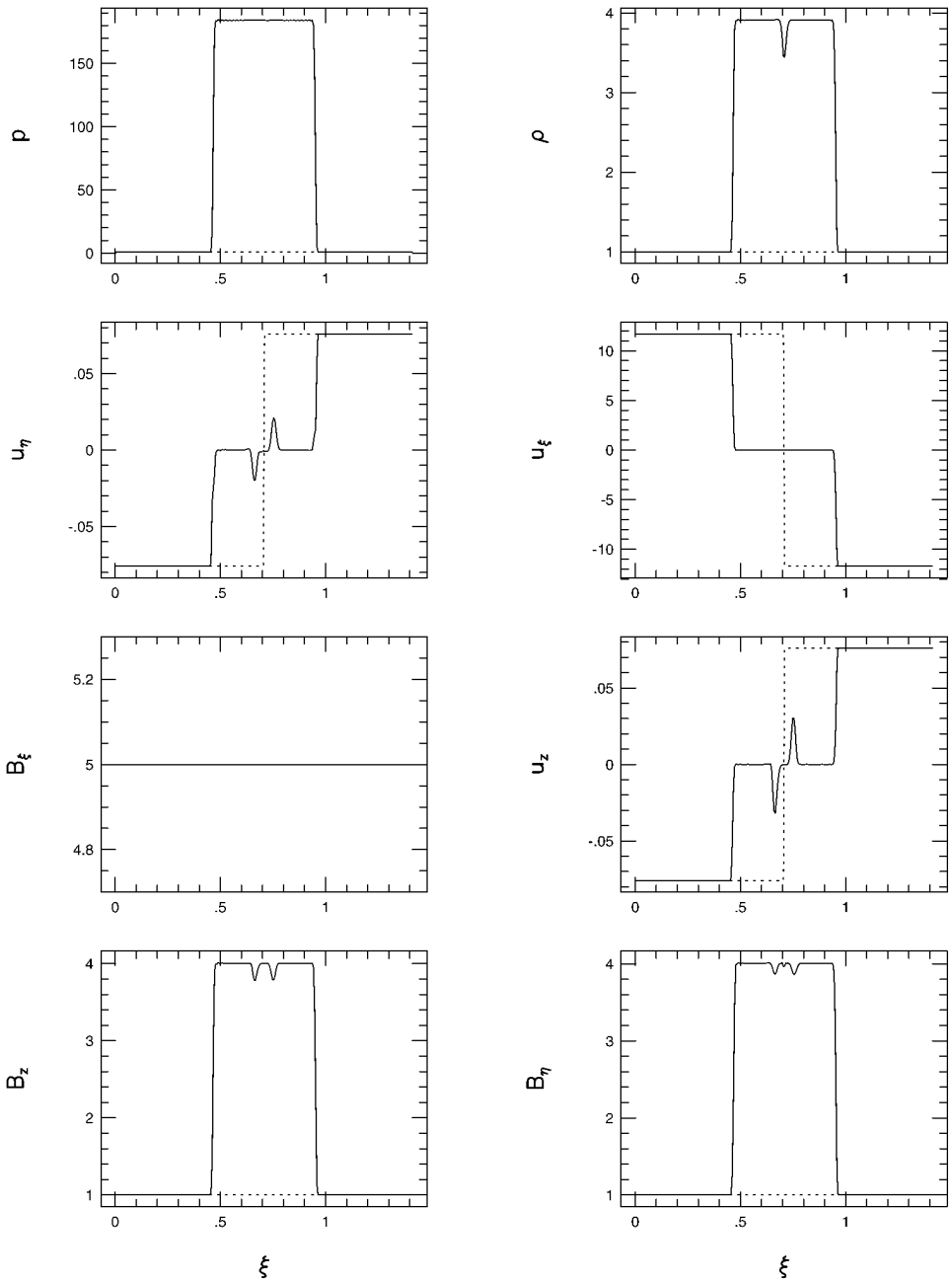

FIG. 4.—Shock-tube problem in a two-dimensional domain. $B_\xi = 5$. The initial condition along the ξ-direction is shown by dashed lines, which is exactly the same as that in Fig. 3. Solid lines are the profiles at $t = 0.06$, which contain two fast shocks.

structure. After the interpolation, we have to find the effective left and right states for the Riemann problem arising from each interface between grid cells. Unlike Godunov schemes for Lagrangian hydrodynamics, the left (or right) state in a single-step Eulerian scheme may come from the cell structure of the right (or left) cell of the interface for supersonic flows.

As an example, here we describe the calculation for the left state of fast waves. If $(u_{xi-1} + c_{fi-1}) \geq 0$ and $(u_{xi} + c_{fi}) \geq 0$, then we consider the domain-average on the domain $x_{i-1} - (u_{xi-1} + c_{fi-1})\Delta t < x \leq x_i$ the left state for fast waves. If $(u_{xi-1} + c_{fi-1}) < 0$ and $(u_{xi} + c_{fi}) < 0$, then we consider the state at the domain-average on the domain $x_i < x < (u_{xi} + c_{fi})\Delta t$ the left state. If $(u_{xi-1} + c_{fi-1}) \geq 0$ and $(u_{xi} + c_{fi}) < 0$, then we consider the average state of the two domain-averages with weighting factors $(u_{xi-1} + c_{fi-1})$ and $|u_{xi} + c_{fi}|$ the left state. If $(u_{xi-1} + c_{fi-1}) < 0$ and $(u_{xi} + c_{fi}) \geq 0$, we are in the middle of a rarefaction fan. In this case, we consider the average of two states in the $(i-1)st$ and ith cells with weighting factors $(u_{xi} + c_{fi})$ and $|u_{xi-1} + c_{fi-1}|$ the left state for fast waves. The left states for Alfvén waves and slow waves, and the right states for fast waves; Alfvén waves and slow waves are similarly calculated. We should point out that if the left (or right) states for different waves were treated as the same, the resulting scheme would be only first-order accurate.

After we obtain the effective left and right states, we approximately solve the Riemann problem (Dai & Woodward 1994c) to calculate the time-averaged flux. The time-averaged density at the interface is approximately calculated through the characteristic formulation for the entropy wave.

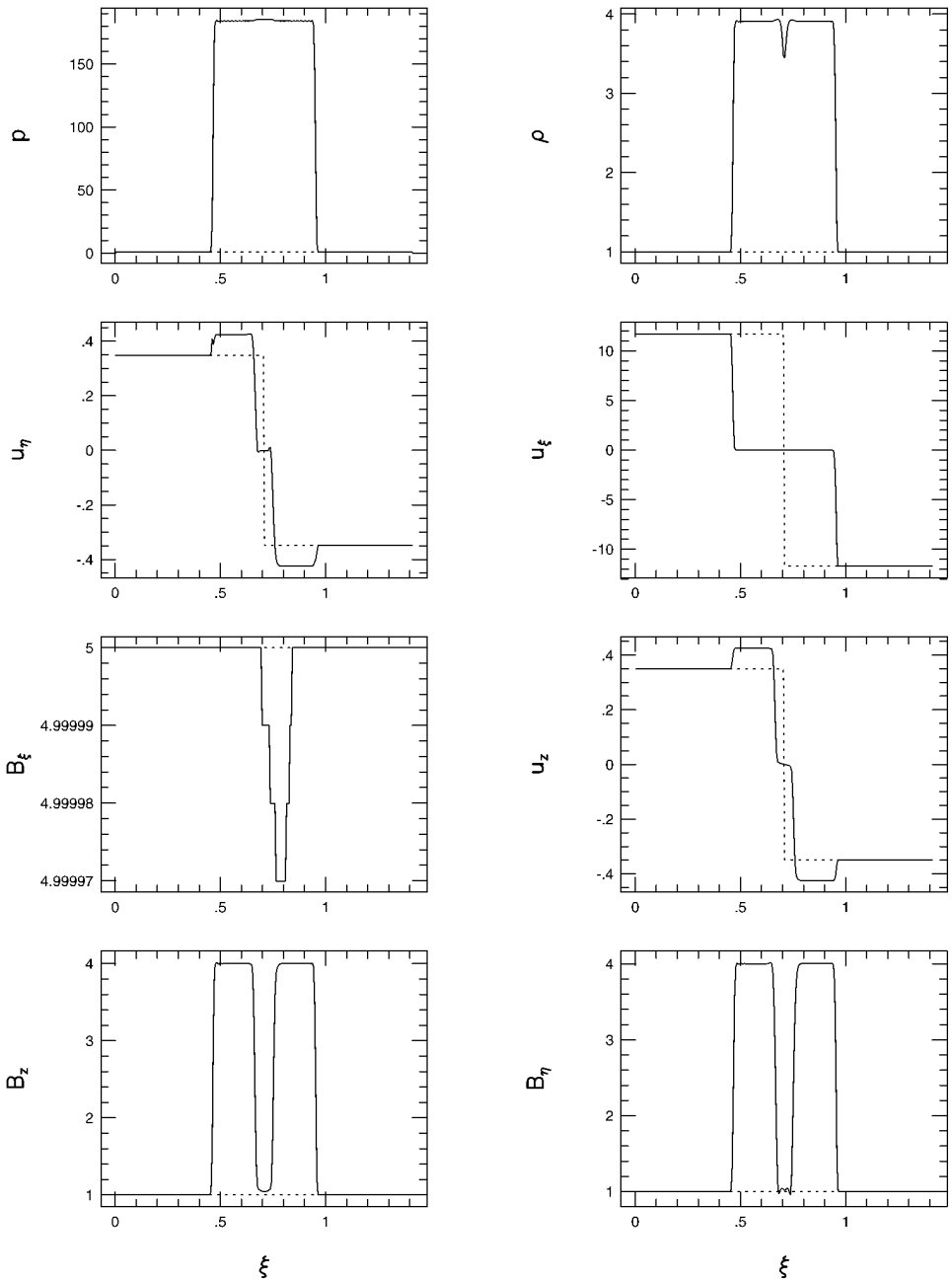

FIG. 5.—Shock-tube problem in a two-dimensional domain. $B_\xi = 5$. The initial condition along the ξ-direction is shown by the dashed lines, which is exactly the same as that in Fig. 4. Solid lines are the profiles at $t = 0.06$, which contain two fast shocks and two slow shocks.

In our current algorithm for multidimensional problems, the time-averaged flux needed in equations (17)–(19), (24), (25) are approximately calculated using the updated $\boldsymbol{u}_{i,j,k}$ and $\boldsymbol{B}_{i,j,k}$. For the flux needed in equations (17)–(19) for three-dimensional problems, we approximately have

$$\bar{\Omega}_{xi} \approx \Omega_x[\tilde{\boldsymbol{u}}_i^*(y_j, z_k), \tilde{\boldsymbol{B}}_i^*(y_j, z_k)] , \tag{28}$$

$$\bar{\Omega}_{yj} \approx \Omega_y[\tilde{\boldsymbol{u}}_j^*(x_i, z_k), \tilde{\boldsymbol{B}}_j^*(x_i, z_k)] , \tag{29}$$

$$\bar{\Omega}_{zk} \approx \Omega_y[\tilde{\boldsymbol{u}}_k^*(x_i, y_j), \tilde{\boldsymbol{B}}_k^*(x_i, y_j)] . \tag{30}$$

Here $\tilde{\boldsymbol{u}}_i^*(y_j, z_k)$, $\tilde{\boldsymbol{u}}_j^*(x_i, z_k)$, and $\tilde{\boldsymbol{u}}_k^*(x_i, y_j)$ are defined as

$$\tilde{\boldsymbol{u}}_i^*(y_j, z_k) \equiv \tfrac{1}{2}[\tilde{\boldsymbol{u}}_i(y_j, z_k, \Delta t) + \tilde{\boldsymbol{u}}_i(y_j, z_k, 0)] ,$$

$$\tilde{\boldsymbol{u}}_j^*(x_i, z_k) \equiv \tfrac{1}{2}[\tilde{\boldsymbol{u}}_j(x_i, z_k, \Delta t) + \tilde{\boldsymbol{u}}_j(x_i, z_k, 0)] ,$$

$$\tilde{\boldsymbol{u}}_k^*(x_i, y_j) \equiv \tfrac{1}{2}[\tilde{\boldsymbol{u}}_k(x_i, y_j, \Delta t) + \tilde{\boldsymbol{u}}_k(x_i, y_j, 0)] ,$$

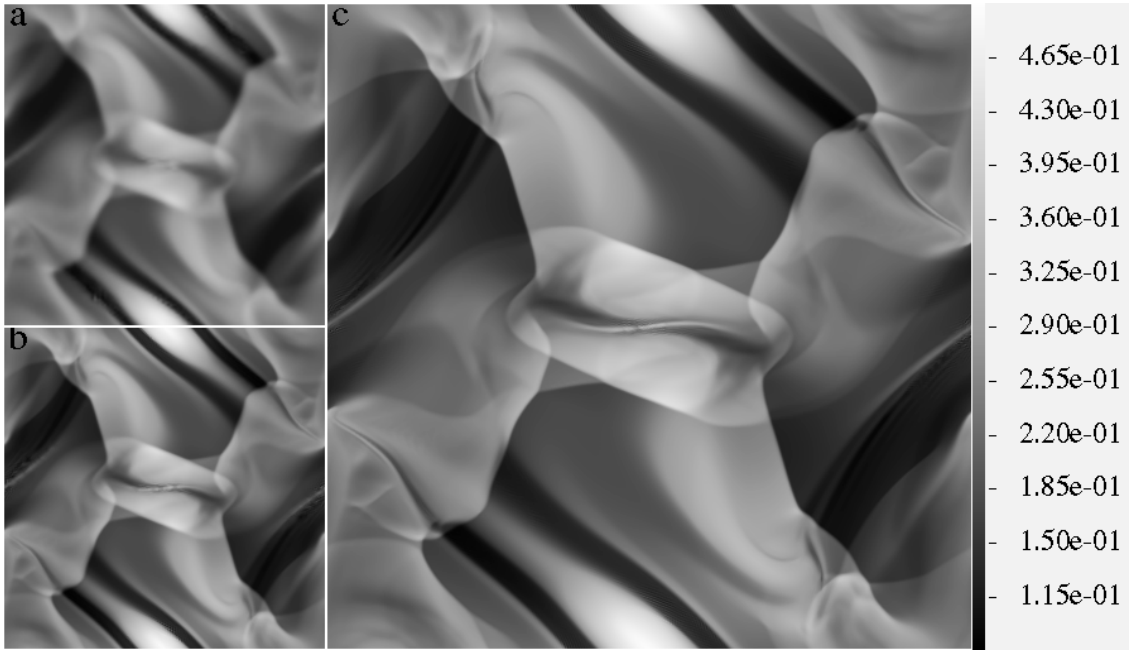

FIG. 6.—Mass density at $t = 0.5$ in the Orszag-Tang vortex system obtained from three simulations with different resolutions: (*a*) 128 × 128, (*b*) 256 × 256, and (*c*) 512 × 512.

and $\tilde{\boldsymbol{u}}_i(y_j, z_k)$ [or $\tilde{\boldsymbol{u}}_j(x_i, z_k)$, or $\tilde{\boldsymbol{u}}_k(x_i, y_j)$] is the average of $\boldsymbol{u}$ along the line $x_{i-1} < x < x_i$, $y = y_j$ and $z = z_k$ (or the line $y_{j-1} < y < y_j$, $x = x_i$ and $z = z_k$, or the line $z_{k-1} < z < z_k$, $x = x_i$ and $y = y_j$). These line averages of $\boldsymbol{u}$ and $\boldsymbol{B}$ at $t = \Delta t$ may be approximately calculated through $\boldsymbol{u}_{i,j,k}(\Delta t)$ and $\boldsymbol{B}_{i,j,k}(\Delta t)$.

For the flux needed in equations (24) and (25) for two-dimensional problems, we approximately have

$$\bar{\Omega}_z(x_i, y_j) \approx \Omega_z[\bar{\boldsymbol{u}}(x_i, y_j), \bar{\boldsymbol{B}}(x_i, y_j)] \ .$$

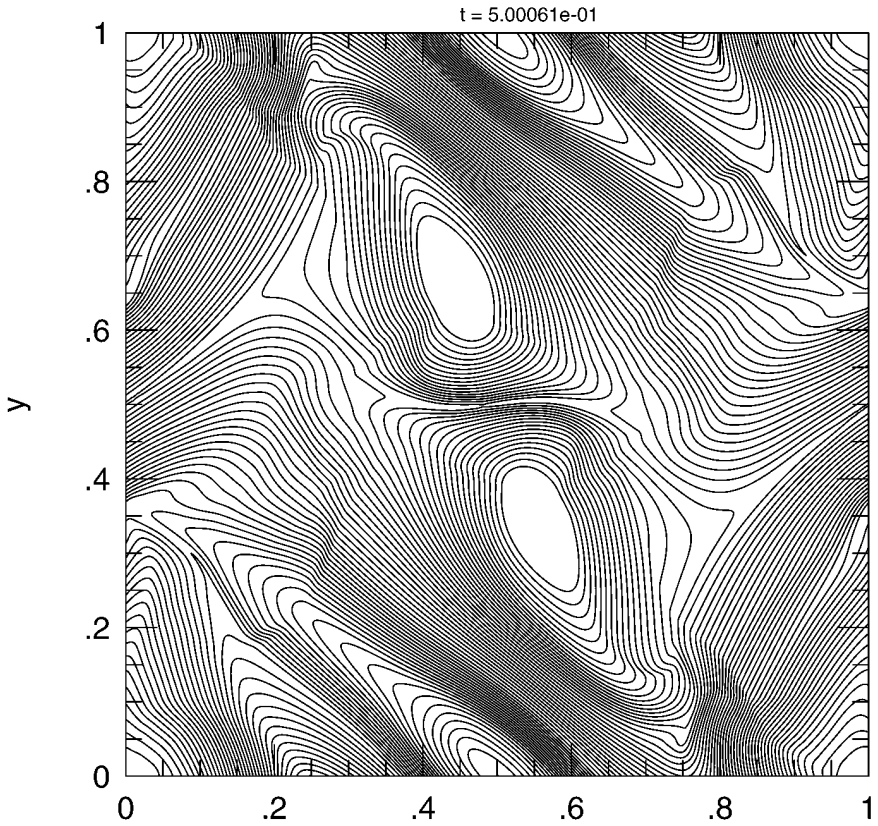

FIG. 7.—Magnetic field lines at $t = 0.5$ in the Orszag-Tang vortex system

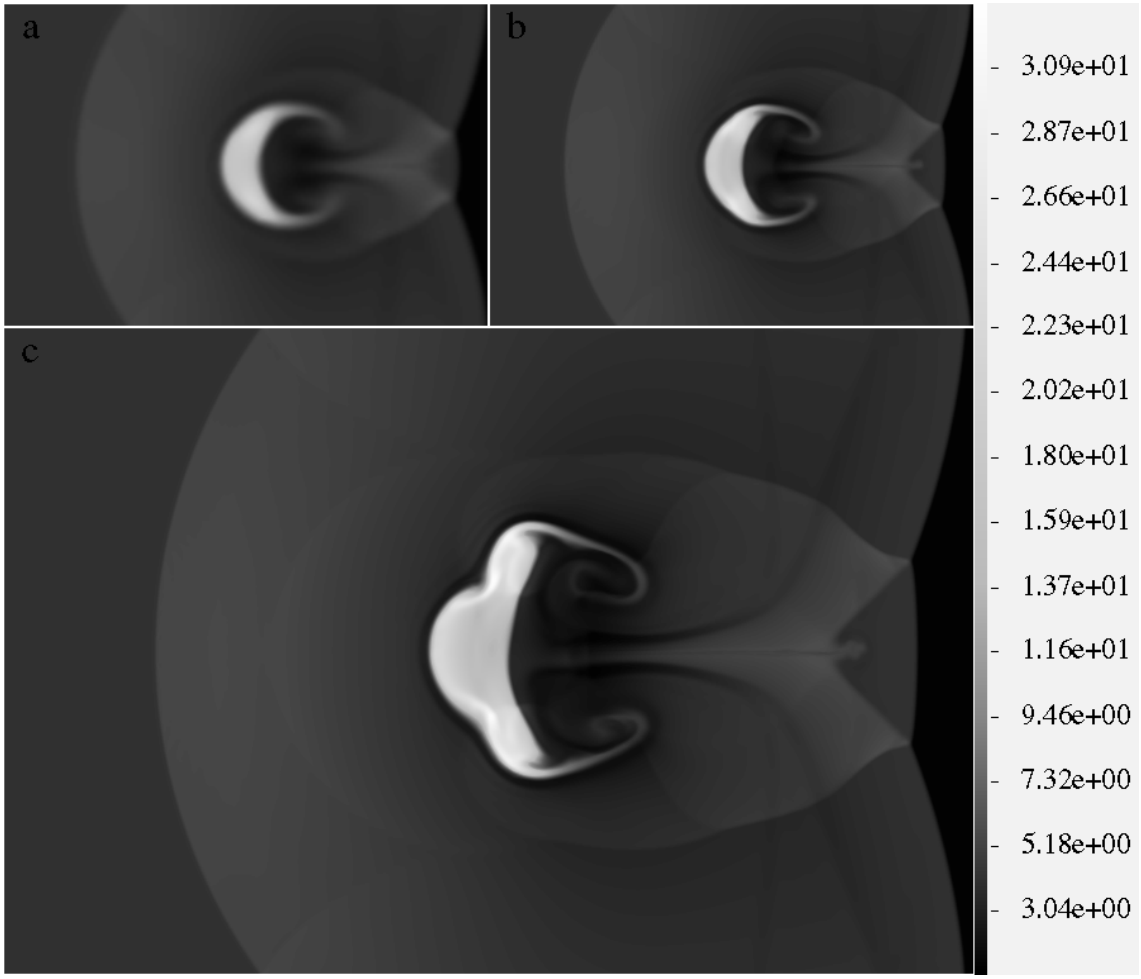

FIG. 8.—Mass density in the interaction between a Mach 15 MHD fast shock and a circular denser plasma cloud. The results are obtained through (*a*) 192 × 128, (*b*) 384 × 256, and (*c*) 768 × 512 grid cells.

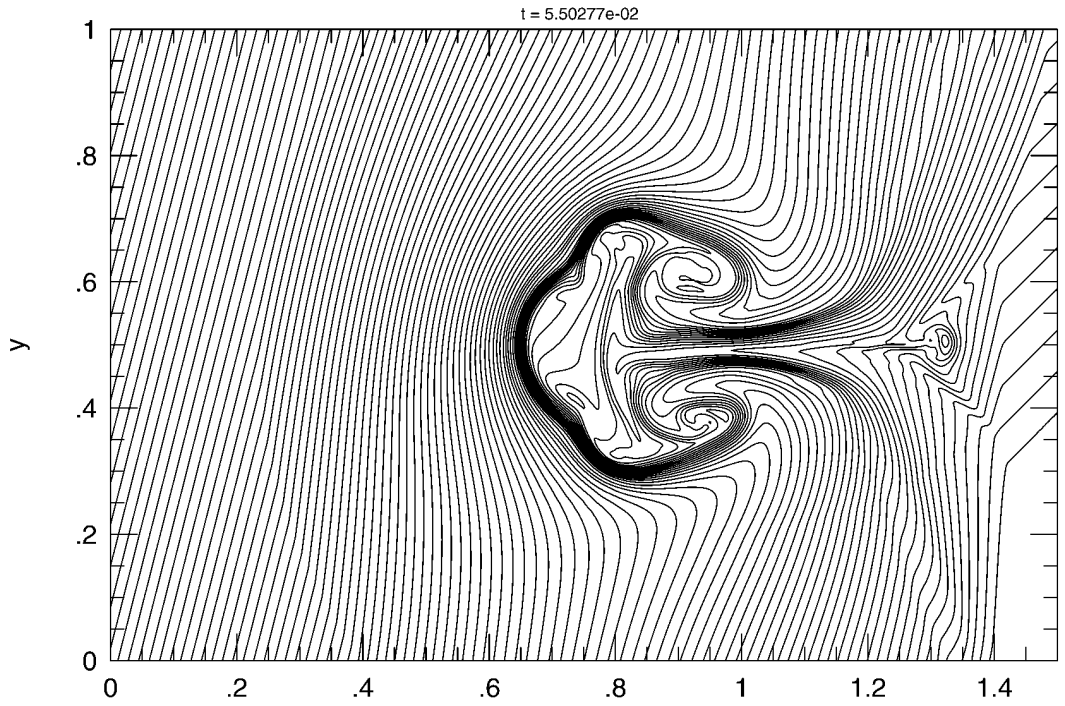

FIG. 9.—Magnetic field lines during the interaction between a Mach 15 MHD fast shock and a denser cloud at $t = 0.055$

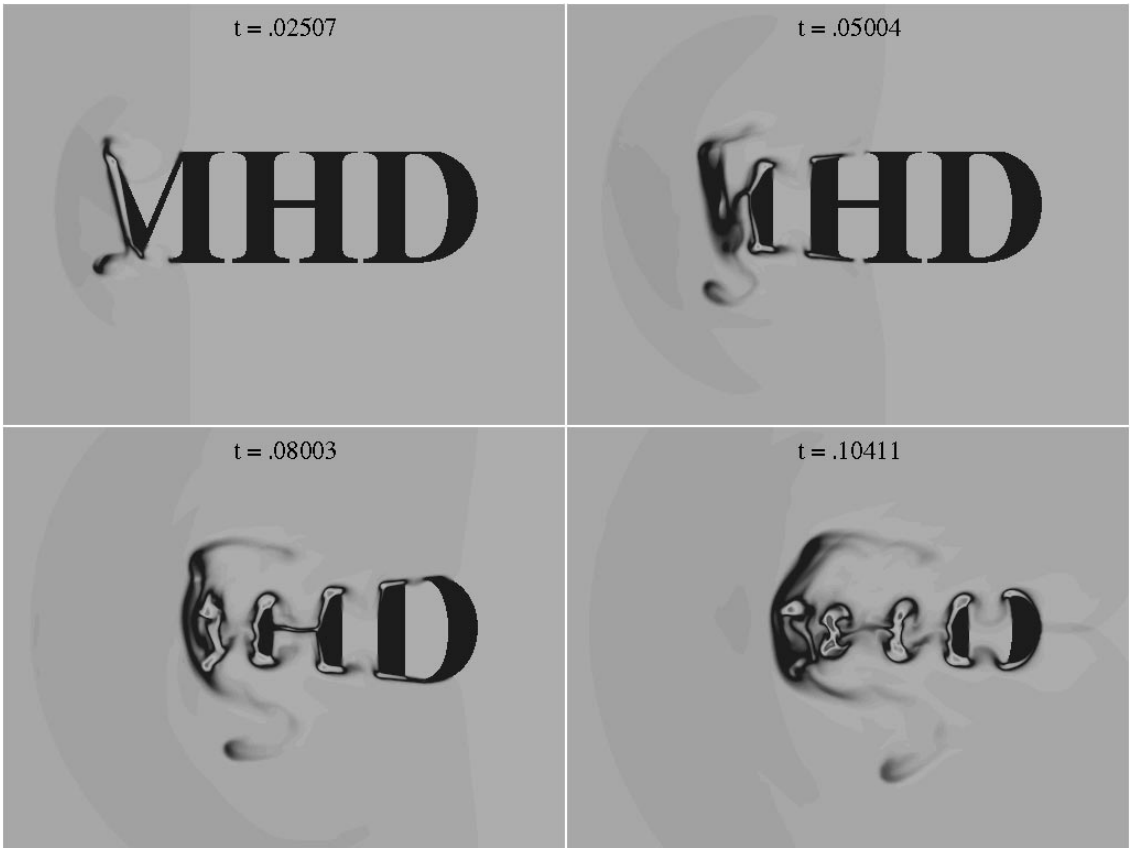

FIG. 10.—Mass density at four instants during the interaction between a MHD fast shock with a set of denser plasma clouds represented by three characters "MHD."

Here $\bar{\boldsymbol{u}}(x_i, y_j)$ and $\bar{\boldsymbol{B}}(x_i, y_j)$ may be approximately calculated through

$$\bar{\boldsymbol{u}}(x_i, y_j) \approx \tfrac{1}{2}[\boldsymbol{u}(x_i, y_j, \Delta t) + \boldsymbol{u}(x_i, y_j, 0)] ,$$

$$\bar{\boldsymbol{B}}(x_i, y_j) = \tfrac{1}{2}[\boldsymbol{B}(x_i, y_j, \Delta t) + \boldsymbol{B}(x_i, y_j, 0)] .$$

The point values $\boldsymbol{u}(x_i, y_j, \Delta t)$ and $\boldsymbol{B}(x_i, y_j, \Delta t)$ may be approximately obtained:

$$\boldsymbol{u}(x_i, y_j, \Delta t) \approx \tfrac{1}{4}[\boldsymbol{u}_{i,j}(\Delta t) + \boldsymbol{u}_{i-1,j}(\Delta t) + \mathbf{u}_{i,j-1}(\Delta t) + \boldsymbol{u}_{i-1,j-1}(\Delta t)] , \tag{31}$$

$$\boldsymbol{B}(x_i, y_j, \Delta t) \approx \tfrac{1}{4}[\boldsymbol{B}_{i,j}(\Delta t) + \boldsymbol{B}_{i-1,j}(\Delta t) + \boldsymbol{B}_{i,j-1}(\Delta t) + \boldsymbol{B}_{i-1,j-1}(\Delta t)] . \tag{32}$$

3. NUMERICAL EXAMPLES

The numerical scheme described in the last section has been tested for some one- and two-dimensional problems for its correctness, accuracy, and robustness, a few two-dimensional simulations are presented here to illustrate the features of the scheme. Actually, $b_{xi,j}$ and $b_{yi,j}$ in our scheme are integrals of B_x and B_y along interfaces. Therefore, from $b_{xi,j}$ and $b_{yi,j}$, we may obtain the z-component of a vector potential $\boldsymbol{A}$ without involving any approximation. Here $(B_x, B_y) = \nabla \times \boldsymbol{A}$. The contours of A_z are exactly magnetic field lines. If the values of the contours are uniformly spaced, the magnitude of (B_x, B_y) is proportional to the density of the magnetic field lines. The magnetic field lines to be reported in this section are obtained through the contours of A_z.

Uniform grids and 5/3 for γ are used in all the examples. Courant numbers used in these examples are around 0.6. We would like to mention again that the net magnetic flux across each numerical cell is exactly the same as its initial value all the time in these simulations.

The first set of examples are for the propagation of MHD waves in a two-dimensional domain, through which the correctness and accuracy of our scheme may be tested for smooth flows. The initial flows are purely one-dimensional in a ξ-direction, which makes an angle α ($\alpha = 30°$) with the x-axis. The simulations are performed in the domain $(L_x - 0) \times (L_y - 0)$, where $L_x = 1/\cos\alpha$ and $L_y = 1/\sin\alpha$, so that periodic boundary conditions may be used. Initial waves, which are propagating along the ξ-direction instead of the x-direction, are set up in the simulation domain. The plots to be presented here are the profiles along $y = L_y/2$.

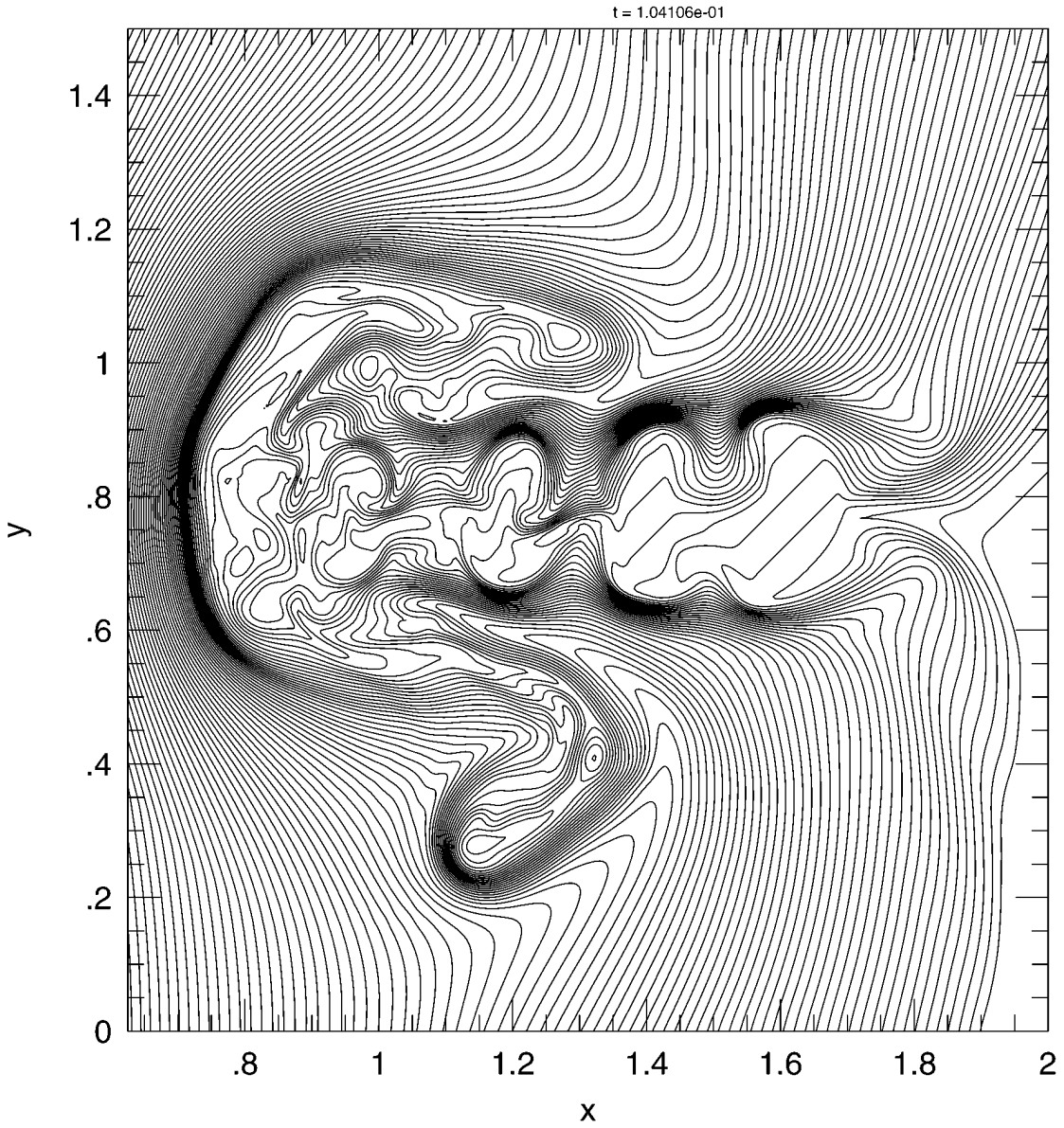

FIG. 11.—Magnetic field lines during the interaction between a MHD fast shock with clouds represented by "MHD" at $t = 0.10411$

The first example is to test the accuracy of our two-dimensional formulations. The dashed lines in Figure 1 are the initial profiles which represent a fast wave propagating in the ξ-direction. The fast wave speed along the ξ-direction is very close to unity, and the solid lines in Figure 1 are the results at $t = 10$ when 128×128, 64×64, 32×32, 16×16, and 8×8 grid cells are used. The second example is for the propagation of a nonlinear fast wave along the ξ-direction. The dashed lines in Figure 2 are initial profiles. The solid lines in Figure 2 are the profiles at $t = 1.0$, 2.0, 3.0, 4.0, and 5.0 obtained when 128×128 grid cells are used.

The next three examples are shock-tube problems in a two-dimensional 1×1 domain, through which the correctness and robustness of our scheme may be tested for discontinuous MHD flows. The initial flows are purely one-dimensional in a ξ-direction, which makes an angle $\alpha = 45°$ with the x-axis. 256×256 grid cells are used in the simulation domain. We should mention that we choose $\alpha = 45°$ only because it is easy to set initial conditions which exactly satisfy the divergence-free condition. Actually, these shock-tube problems do not have a symmetry between x- and y-axes because of the component of magnetic field in the η-direction. The η-direction is the one perpendicular to both the ξ- and the z-directions.

The first shock-tube problem in a two-dimensional domain is to examine the conservation laws for a shock propagating at the ξ-direction. The initial shock along the ξ-direction is shown by the dashed lines in Figure 3. The solid lines in Figure 3 show the profiles at $t = 0.06$ along the line $y = x$, where $B_\xi \equiv b_{xi,j} \cos \alpha + b_{y,i,j} \sin \alpha$, and $B_\eta \equiv b_{y,i,j} \cos \alpha - b_{xi,j} \sin \alpha$. Grid cells of 256×256 are used in the simulation domain. Notice that the jump conditions, which represent the conservation laws, are satisfied across the shock. We would like to mention that there would be $O(1)$ truncation errors in the jump conditions if the scheme were not conservative for any one of eight conserved quantities. We should point out that there exist "starting errors" (Dai & Woodward 1994b) in the numerical results. The starting errors result from the purely discontinuous

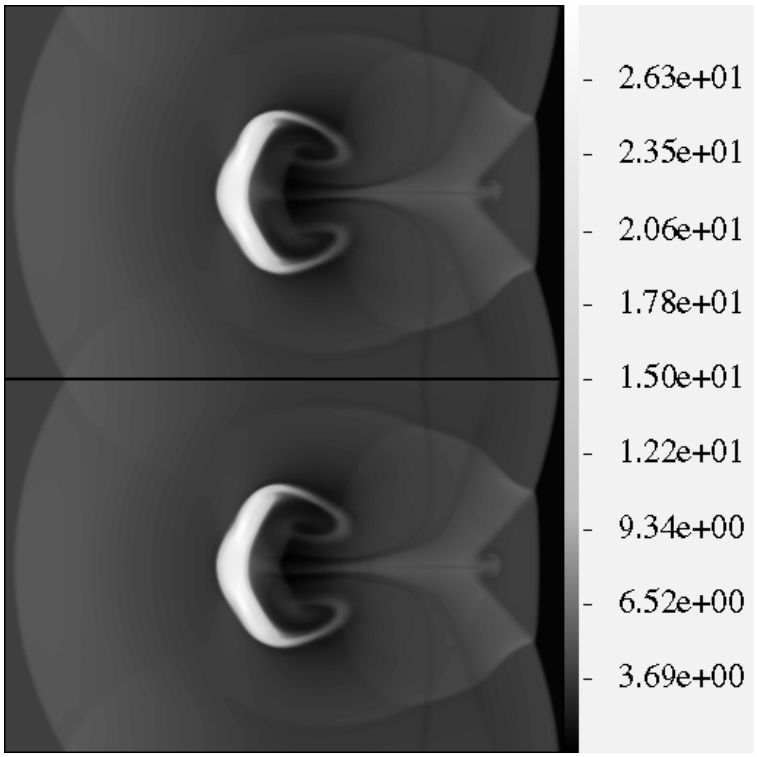

FIG. 12.—Comparison in the mass density between two numerical methods for the interaction between a Mach 15 MHD fast shock and a denser cloud. The upper image is obtained through the scheme with divergence-free constraint exactly satisfied; the lower image is obtained with the constraint satisfied to the second-order accuracy. The magnitude and structure shown in the two images are very close.

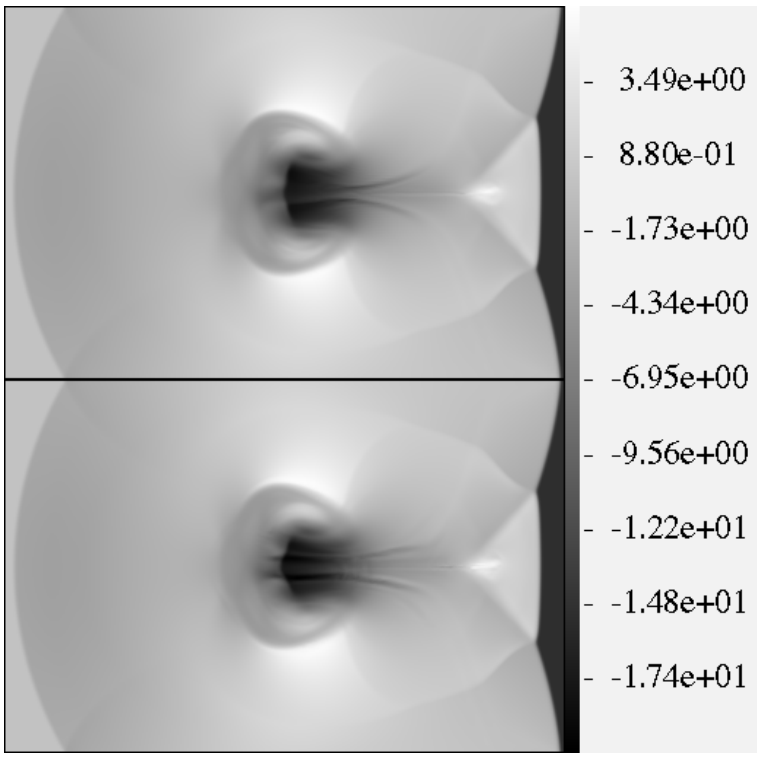

FIG. 13.—Comparison in the x-component of flow velocity between two methods for the interaction between a Mach 15 MHD fast shock and a denser cloud. The upper image is obtained through the scheme with divergence-free constraint exactly satisfied; the lower image is obtained with the constraint satisfied to the second-order accuracy. There are differences near the center of cloud and in the tail behind the cloud.

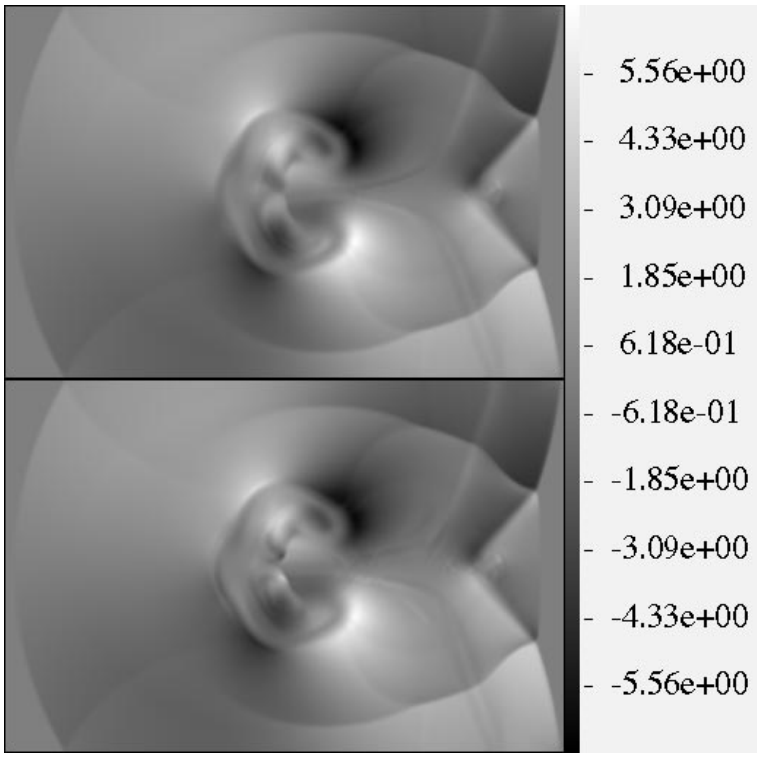

FIG. 14.—Comparison in the *y*-component of flow velocity between two methods for the interaction between a Mach 15 MHD fast shock and a denser cloud. The upper image is obtained through the scheme with divergence-free constraint exactly satisfied; the lower image is obtained with the constraint satisfied to the second-order accuracy.

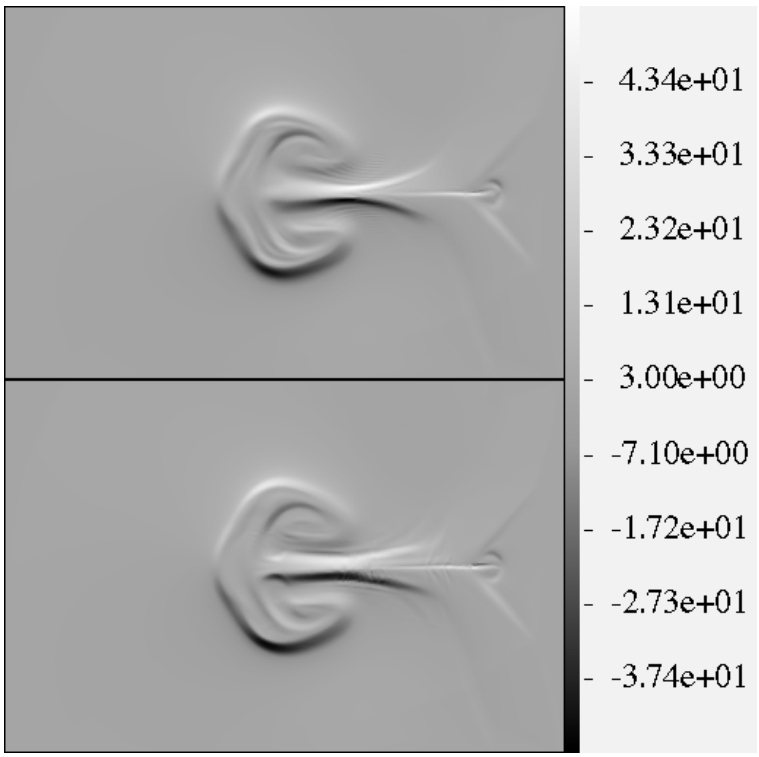

FIG. 15.—Comparison in the *x*-component of magnetic field between two methods for the interaction between a Mach 15 MHD fast shock and a denser cloud. The upper image is obtained through the scheme with divergence-free constraint exactly satisfied; the lower image is obtained with the constraint satisfied to the second-order accuracy. Two images are very close except that the upper image in more clean in the tail behind the cloud.

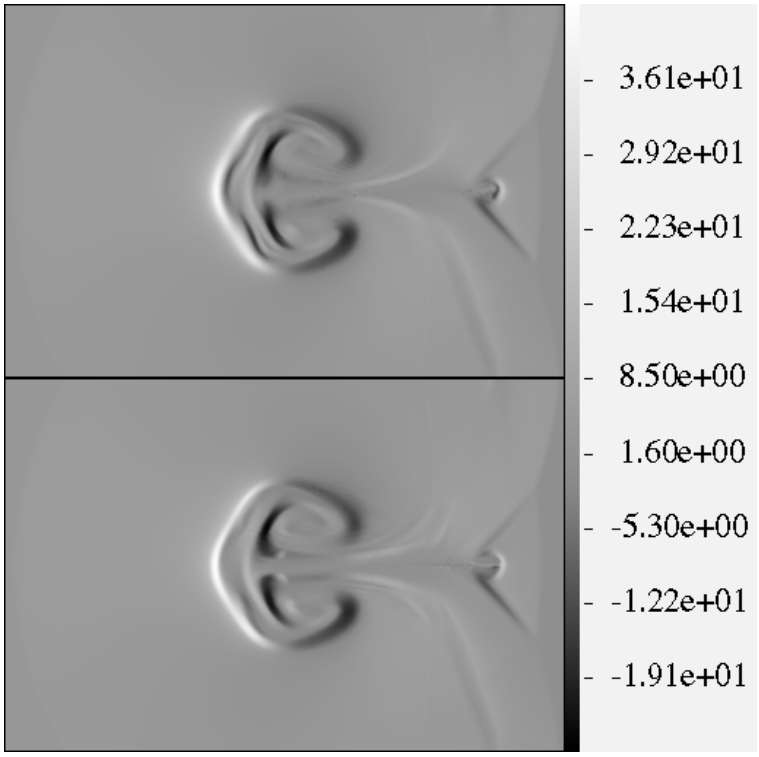

FIG. 16.—Comparison in the y-component of magnetic field between two methods for the interaction between a Mach 15 MHD fast shock and a denser cloud. The upper image is obtained through the scheme with divergence-free constraint exactly satisfied; the lower image is obtained with the constraint satisfied to the second-order accuracy. Two images are close except near the front of the cloud.

initial condition. If the initial shock is given a very small internal structure, the starting errors will disappear. In the remaining numerical examples, purely discontinuous profiles are always given for discontinuous initial conditions. Therefore, the simulation results may contain starting errors, and we will not point out the start errors again.

The profiles along the line $y = x$ at $t = 0.06$ in the next two shock-tube problems in a two-dimensional domain are given in Figures 4 and 5. The dashed lines in Figures 4 and 5 are the initial conditions. The profiles in Figure 4 contain two fast shocks with Mach number 10 each; the profiles in Figure 5 show two fast shocks and two slow shocks. We should point out that the

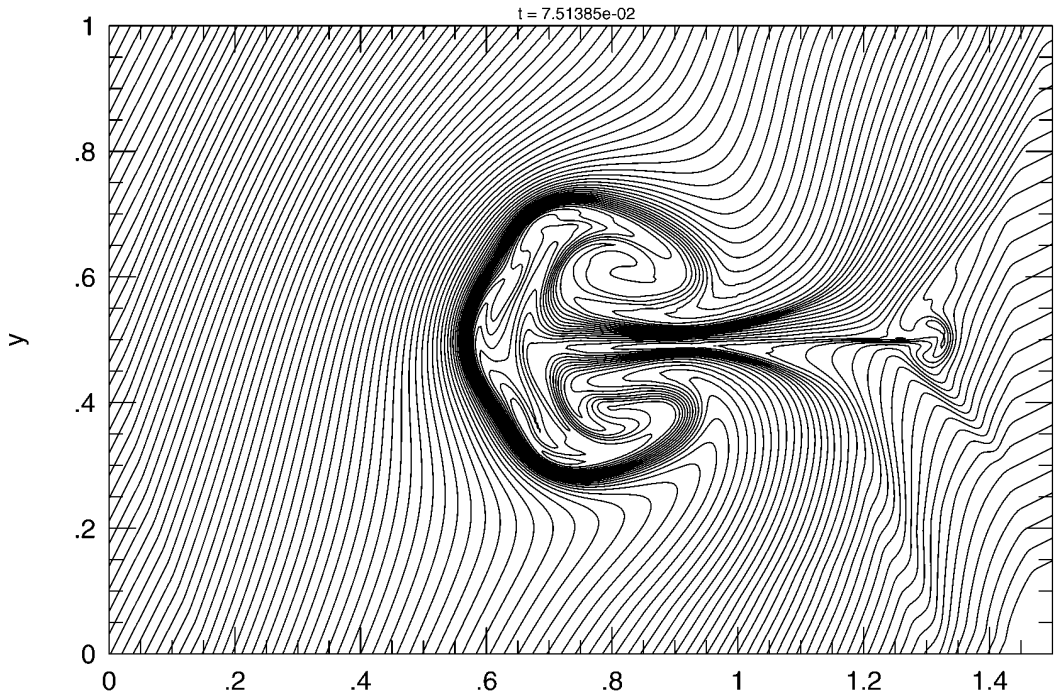

FIG. 17.—Magnetic field lines at one instant for the interaction between a Mach 15 MHD fast shock and a denser cloud

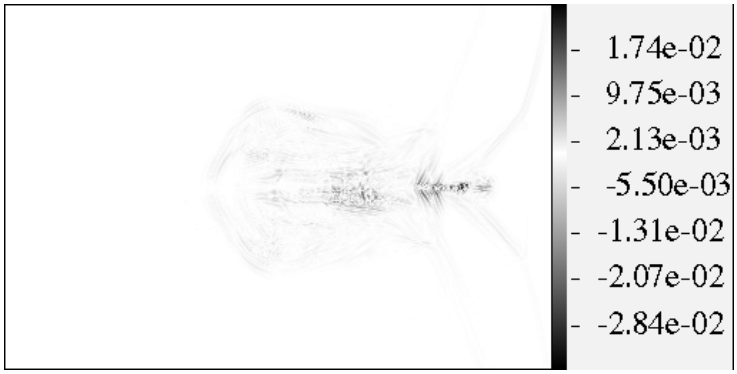

FIG. 18.—Magnitude of the net magnetic flux through each grid cell in a simulation for the interaction between a Mach 15 MHD fast shock and a denser cloud. The divergence-free constraint is kept only to the second order of accuracy in the simulation.

scheme does not have mechanisms to maintain the constant B_ξ in the three shock-tube problems in the two-dimensional domain, and the variation in B_ξ is a symptom of truncation errors.

The next two-dimensional example is the Orszag-Tang vortex problem, which was first studied by Orszag & Tang (1979) for incompressible MHD flows. The numerical investigation of the Orszag-Tang vortex system for compressible flows was carried out by Dahlburg & Picone (1989) and Picone & Dahlburg (1991). The initial conditions for this system consist of nonrandom, periodic fields in which the magnetic field and flow velocity contain X points but differ in their modal structures along one spatial direction. The initial conditions used in our example are

$$\rho(x, y) = \rho_0 , \qquad p(x, y) = p_0 ,$$
$$\boldsymbol{u}(x, y) = -\sin(2\pi y)\boldsymbol{i} + \sin(2\pi x)\boldsymbol{j} , \qquad \boldsymbol{B}(x, y) = -\sin(2\pi y)\boldsymbol{i} + \sin(4\pi x)\boldsymbol{j} .$$

Here $\boldsymbol{i}$ and $\boldsymbol{j}$ are unit vectors in x- and y-directions. The constants p_0 and ρ_0 in the initial conditions are determined through an averaging β_0 and an averaging Mach number M_0, which are defined as

$$\beta_0 \equiv \frac{p_0}{\langle \boldsymbol{B}^2 \rangle / 8\pi} = 8\pi p_0 , \qquad M_0 \equiv \frac{\langle \boldsymbol{u}^2 \rangle}{\gamma p_0 / \rho_0} = \frac{\rho_0}{\gamma p_0} .$$

In this example, $\beta_0 = 10/3$ and $M_0 = 1$ are used. Our simulations for this problem are performed in an 1×1 domain in which three grids with 128×128, 256×256, and 512×512 cells are used. Figure 6 shows the mass density at $t = 0.5$, and Figure 7 shows the magnetic field lines at that moment.

The next two-dimensional example is for the interaction between MHD fast shock and a denser plasma cloud. Interactions between MHD shocks and denser clouds have been numerically studied (Dai & Woodward 1995; Jones & Kang 1993; Jones, Ryu, & Tregellis 1996; Mac Low et al. 1994; Mac Low & Zahnle 1994) for astrophysics problems. As a practical test problem, we set up a problem involving all three components of the magnetic field in the simulation, initially, an MHD fast shock propagating in the x-direction with a Mach number 15. The preshock state for $(\rho, p, u_x, u_y, u_z, B_x, B_y, B_z)$ is (1, 1, 0, 0, 0, 2, 2, 2), and the postshock state is (3.94258, 399.481, 17.3463, −0.040403, −0.040403, 2, 7.89899, 7.89899). The simulation is performed in a (1.5–0) × (1–0) domain in which three grids with 192×128, 384×256, and 768×512 are used. In the front of the shock, there is initially a circular cloud, the center and radius of which are (0.375, 0.5) and 0.15. The cloud is 10 times denser than the plasma at the preshock state. Figure 8 shows the mass density at one moment, and Figure 9 shows the

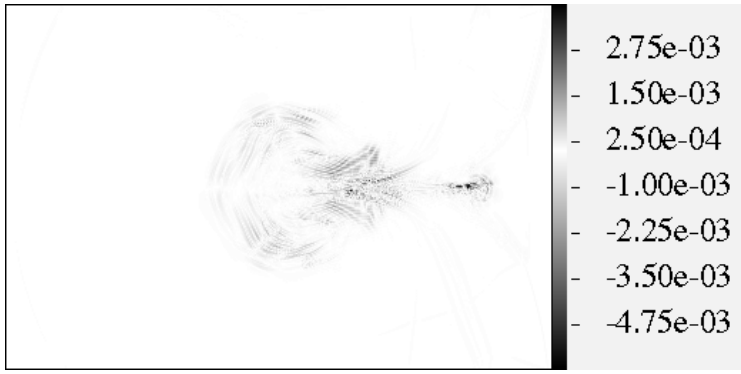

FIG. 19.—Magnitude of the net flux through each grid cell at one instant for the interaction between a Mach 15 MHD fast shock and a denser cloud. The net flux is calculated from cell-averaged $\boldsymbol{B}_{i,j,k}$ instead of interface-averaged $\boldsymbol{B}_{i,j,k}$.

magnetic field lines at that moment. Each image in Figure 8 shows the mass density obtained from one grid.

The next example is about the interaction between a Mach 12 MHD fast shock and a set of clouds. The preshock state of the fast shock for (ρ, p, u_x, u_y, u_z, B_x, B_y, B_z) is (1, 1, 0, 0, 0, 2, 2, 2), and the postshock state is (3.91109, 253.724, 13.8388, -0.00500, -0.00500, 2, 7.84323, 7.84323). The clouds are represented by three characters MHD in front of the shock. Within the three characters, $\rho = 50$, and other variables have the same values as those at the preshock state. This simulation is implemented in a (2–0) $\times$ (1.5–0) domain with 512 $\times$ 384 grid cells to test the robustness of the scheme. Figure 10 shows the mass density at four instants, and Figure 11 shows the magnetic field lines at one instant.

As discussed before, in the existing Godunov schemes, there are no mechanisms to keep the divergence of the magnetic field small. It is obvious that the implementation of the divergence-free condition in an existing scheme may produce different numerical solutions. But it remains unknown whether or not truncation errors in the divergence-free constraint, which may be not small for supersonic flows, in the existing Godunov schemes have serious influences on the dynamics if conservation laws are exactly satisfied. We have compared two approaches in numerical solutions, one with the operator $D_{\Delta t}$ and the other without $D_{\Delta t}$, for a few MHD problems. Two solutions obtained from the two approaches are not significantly different, although some differences exist in small scales. Here we present the comparison for the interaction between an MHD fast shock and a denser cloud. The Mach number of the initial fast shock in this problem is 15, and the cloud is 10 times denser than the preshock state. The pre- and postshock states for (ρ, p, u_x, u_y, u_z, B_x, B_y, B_z) are (1, 1, -15.2677, 0, 0, 2, 1, 1) and (3.94605, 312.063, 0, -0.0229969, -0.0229969, 2, 3.95492, 3.95492). The simulations are performed in a domain (1.5–0) $\times$ (1–0) with 384 $\times$ 256 grid cells. We have examined the differences between two solutions in all the independent variables, ρ, E, $\boldsymbol{u}$, and $\boldsymbol{B}$. We would like to say that the two solutions are very close, although differences may be found both in structures and magnitudes. The comparison of some of the variables is presented here. Figure 12 shows the comparison in mass density. It is very hard to find differences between two images in either structure and magnitude. Figure 13 shows the comparison in the x-component of flow velocity. There are differences near the center of cloud and in the tail behind the cloud. Figure 14 shows the comparison in the y-component of the flow velocity. Some differences may be found near the center of the cloud and in the tail of the cloud. Figure 15 shows the comparison in B_x, and two images are very close except that the upper image is more clean in the tail behind the cloud. Figure 16 gives the comparison in B_y, the two images are close except near the front of the cloud. As discussed before, the magnetic field in the proposed scheme is divergence-free. Figure 17 shows the magnetic field lines at one instant for the problem. It is clear that there is a shear layer in the tail behind the cloud, where the two solutions are most different. In the other simulation, the divergence-free constraint is kept to the second order of accuracy, and Figure 18 shows the net magnetic flux through each grid cell. It is easy to see that the magnitude of the net flux is relatively large in the places where two solutions are different, specially in the tail behind the cloud. The net flux shown in Figure 18 are calculated from cell averages of the magnetic field through interpolation.

4. CONCLUSIONS AND DISCUSSION

In this paper, an approach to exactly maintain both the eight conservation laws and the divergence-free condition has been proposed for multidimensional MHD equations, and a second-order finite difference scheme based on the approach and an approximate MHD Riemann solver has been presented. Compared to existing Godunov schemes for MHD equations, the scheme presented in this paper is simple. The scheme may be used to study supersonic MHD problems.

In the approach proposed in this paper, the three components of the magnetic field are defined at three sets of interfaces. Therefore, the grid proposed in the paper is staggered. But, the staggered grid proposed here is different from traditional staggered grids in which flow variables are defined at different sets of grids. But in our approach, flow variables $\boldsymbol{W}_{i,j,k}$ are defined at the same grid. Generally, face averages and staggered grids are not favored in hyperbolic systems of conservation laws. But, the conservation law for any component of the magnetic field is very special, in which derivatives in one spatial direction disappear. It is is this feature that make the face averages and the staggered grid are particularly useful in the numerical scheme for MHD flows.

As in existing Godunov schemes, cell-averaged fields, $\boldsymbol{B}_{i,j,k}$, in the proposed scheme do not exactly maintain the divergence-free constraint. If the divergence has to be calculated from cell-averaged fields $\boldsymbol{B}_{i,j,k}$ instead of interface-averaged fields $\boldsymbol{b}_{i,j,k}$, interpolations have to be involved. The actual value of the divergence is interpolation-dependent. For the problems presented in this paper, the maximum magnitude of the divergence is $O(1)$, no matter what kind of interpolation is used to calculate the divergence. We have calculated the net magnetic flux through $\boldsymbol{B}_{i,j,k}$ for the Orszag-Tang problem, the interaction between MHD fast shock and a set of clouds " MHD," and the interaction between an MHD fast shock and a circular cloud, which are described in the last section. Compared to the net magnetic flux obtained from an existing scheme without the operator $D_{\Delta t}$, the magnitude obtained from the proposed scheme is 1 order lower. Here, we give one of the calculations, which is for the interaction between a Mach 15 MHD fast shock and a denser cloud described in Figures (12)–(17). The net magnetic flux calculated from cell-averaged fields $\boldsymbol{B}_{i,j,k}$ is shown in Figure 19. Compared to the magnitude shown in Figure 18, the magnitude shown in Figure 19 is 1 order lower than that in Figure 18, because of the divergence-free constraint implemented in the proposed scheme.

As we discussed before, the cell-averaged fields, $\boldsymbol{B}_{i,j,k}$, are only intermediate variables in our scheme. Since $\boldsymbol{B}_{i,j,k}$ are used only to calculate time-averaged fluxes, the requirements we need for $\boldsymbol{B}_{i,j,k}$ are the same as those for time-averaged fluxes. The $\boldsymbol{B}_{i,j,k}$ should be accurate to the order of the scheme for smooth flows, and $\boldsymbol{B}_{i,j,k}$ should give a reasonable solution if used in Riemann problems in a Godunov scheme. As we know, the solution of a Riemann problem obtained through any approximate Riemann solver in both hydrodynamics and magnetohydrodynamics may be far away from an exact solution for supersonic flows. But approximate Riemann solvers are fine if they are put into conservation laws. For the same reason, we believe that $\boldsymbol{B}_{i,j,k}$ do not necessarily have to exactly satisfy the divergence-free condition, and $\boldsymbol{B}_{i,j,k}$ may be far away from the

condition for supersonic flows. It is the conservation laws which play the crucial role in the simulations for supersonic flows.

As stated before, the approach proposed in this paper may be easily applied to other Godunov schemes for MHD equations, include dimensionally split and unsplit schemes. For unsplit schemes, the time-averaged fluxes needed in equation (6) are calculated simultaneously. Therefore, the time-averaged fluxes may be directly used to calculate the time-averaged fluxes needed in equations (17)–(19), (24), and (25). The proposed approach will look more natural if it is used in unsplit schemes. For split schemes, since x-, y-, and z-sweeps are implemented at different instants, the time-averaged fluxes at three different sets of grid interfaces in equation (6) are obtained at different time. It is not clear whether or not an interpolation may be introduced among these three sets of time-averaged fluxes to calculate the time-averaged fluxes needed in equations (17)–(19), (24), and (25) under the second-order accuracy in time. Finally, we would like to point out that an approximate Riemann solver for fully multidimensional Riemann problems arising from grid points instead of interfaces will be useful for the calculation of time-averaged flux needed in equations (17)–(19), (24), and (25).

The work presented here has been supported by the Department of Energy through grants DE-FG01-87ER25035 and DE-FG02-94ER25207, by the National Science Foundation through grant ASC 93-09829, by NASA through grant USRA/5555-23/NASA, and by the University of Minnesota through its Minnesota Supercomputer Institute.

REFERENCES

Balsara, D. 1996, J. Comput. Phys., submitted
Brackbill, J. U., & Barnes, D. C. 1980, J. Comput. Phys., 35, 426
Brio, M., & Wu, C. C. 1988, J. Comput. Phys., 75, 400
Colella, P. 1990, J. Comput. Phys., 87, 171
Croisille, J.-P., Khanfir, R., & Chanteur, G. 1995, J. Sci. Comput., 10, 81
Dahlburg, R. B., & Picone, J. M. 1989, Phys. Fluid B, 1, 2153
Dai, W., & Woodward, P. R. 1994a, J. Comput. Phys., 111, 354
———. 1994b, J. Comput. Phys., 115, 485
———. 1994c, ApJ, 776, 436
———. 1995, J. Comput. Phys., 121, 51
Evans, C., & Hawley, J. F. 1988, ApJ, 332, 659
Jones, T. W., & Kang, H. 1993, ApJ, 402, 560
Jones, T. W., Ryu, D., & Tregillis, I. L. 1996, preprint
Landau, L. D., & Lifshits, E. 1960, Electrodynamics of Continuous Media (New York: Pergamon)
Mac Low, M., McKee, C. F., Klein, R. I., Stone, J. M., & Norman, M. L. 1994, ApJ, 433, 757
Mac Low, M., & Zahnle, K. 1994, ApJ, 434, L33
Orszag, S. A., & Tang, C.-M. 1979, J. Fluid Mech., 90, 129
Picone, J. M., & Dahlburg, R. B. 1991, Phys. Fluid B, 3, 29
Powell, K. G. 1994, ICASE Rep. No. 94-24
Powell, K. G., Roe, P. L., Myong, R. S., Gombosi, T., & Zeeuw, D. 1995, in Numerical Methods for Fluid Dynamics, ed. K. W. Morton & M. J. Baines (Oxford: Clarendon), 163
Ryu, D., & Jones, T. W. 1995, ApJ, 442, 228
Ryu, D., Jones, T. W., & Frank, A. 1995, ApJ, 452, 785
Saltzman, J. 1994, J. Comput. Phys., 115, 153
Stone, J. M., & Norman, M. L. 1992, ApJ, 80, 791
Strang, G. 1968, SIAM J. Numer. Anal., 5, 506
Zachary, A. L., & Colella, P. 1992, J. Comput. Phys., 99, 341
Zachary, A. L., Malagoli, A., & Colella, P. 1994, SIAM J. Sci. Stat. Comput., 15, 263